J. Fluid Mech. (1991), *vol.* 230, *pp.* 505–524
Printed in Great Britain

Self-induced flow in a rotating tube

By S. GILHAM,† P. C. IVEY,‡ J. M. OWEN¶ AND J. R. PINCOMBE

Thermo-Fluid Mechanics Research Centre, School of Engineering and Applied Sciences, University of Sussex, Falmer, Brighton, BN1 9QT, UK

(Received 30 August 1990)

When a tube, sealed at one end and open to a quiescent environment at the other, is rotated about its axis, fluid flows from the open end along the axis towards the sealed end and returns in an annular boundary layer on the cylindrical wall. This paper describes the first known study to be made of this self-induced flow. Numerical solutions of the Navier–Stokes equations are shown to be in mainly good agreement with experimental results obtained using flow visualization and laser–Doppler anemometry in a rotating glass tube.

The self-induced flow in the tube can be described in terms of the length-to-radius ratio, G, and the Ekman number, E. However, for large values of G ($G \geqslant 20$), the flow outside the boundary layer on the endwall of the tube can be characterized by a single, modified, Ekman number, E^*, where $E^* = GE$. Although most of the fluid entering the open end of the tube is entrained into the annular (Stewartson-type) boundary layer, for small values of E^* ($E^* < 0.2$) some flow reaches the sealed end. For this so-called 'short-tube case', the flow in the boundary layer on the endwall is shown to be similar to that associated with a disk rotating in a quiescent environment: the free disk. The self-induced flow for the short-tube case is believed to be responsible for the 'hot-poker effect' used, on some jet engines, to provide ice protection for the nose bullet.

1. Introduction

Ice formation in the air intake of a jet engine can present a major hazard: large pieces of ice centrifuged from the central portion of the rotating nose cone (or nose bullet) at the front of the engine can be ingested by the compressor, damaging its blades. Ice-protection systems are used to solve this problem, and in one system, used by Rolls Royce, hot air is passed through the hollow compressor shaft of the engine to an anti-icing tube attached to the nose bullet. After impinging on the inner surface of the bullet, the hot air is exhausted through vents (as shown in figure 1), and is liable to be ingested by the compressor. This ingestion can cause a loss of performance and a reduction in the operating surge-margin of the compressor.

Rolls-Royce engineers conducted tests on an anti-icing system in which the vents were sealed to prevent hot-air ingestion into the compressor. They found, somewhat surprisingly, that heat transfer still occurred at the nose bullet even though there was

† Present address: WS Atkins Engineering Sciences Ltd., Woodcote Grove, Ashley Road, Epsom, Surrey, KT18 5BW, UK.

‡ Present address: Department of Turbomachinery and Engineering Mechanics, School of Mechanical Engineering, Cranfield Institute of Technology, Cranfield, Beds, MK43 0AL, UK.

¶ Present address: School of Mechanical Engineering, University of Bath, Claverton Down, Bath, BA2 7AY, UK.

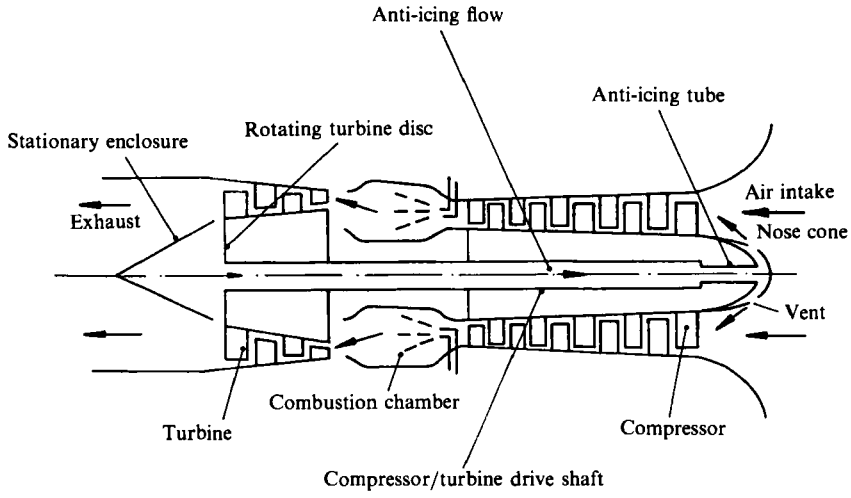

FIGURE 1. Schematic diagram of a jet engine showing the anti-icing system for the nose bullet.

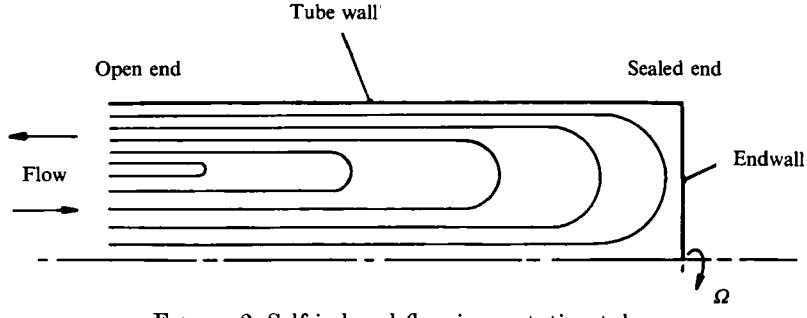

FIGURE 2. Self-induced flow in a rotating tube.

no longer a superposed flow of hot air through the anti-icing tube. This unexpected behaviour was referred to by the engineers as the 'hot-poker effect'.

A pilot study was subsequently conducted by Owen & Pincombe (1981) at the University of Sussex. They carried out flow visualization for a circular glass tube, with a length-to-diameter ratio of around 27, rotating at speeds up to 2000 rev/min. about its axis. One end of the tube was open to the atmosphere and the other end was sealed, to simulate the nose bullet. A laser was used to create slit illumination and smoke, made from micron-size oil particles, was introduced near the open end. The smoke was seen to travel along the axis from the open to the sealed end and to return in an annular layer on the inner wall of the tube. This phenomenon, which was observed under isothermal conditions, was termed 'self-induced flow in a rotating tube'.

Figure 2 shows a simplified diagram of the observed flow. At high rotational speeds, the flow was seen to penetrate the entire length of the tube: this was called the 'short-tube case'. At low speeds, the recirculating flow was confined to a region near the open end: the 'long-tube case'. The strength of the flow was found to depend on both the rotational speed and the length-to-radius ratio of the tube.

The phenomenon of self-induced flow can be readily understood by first considering

a rotating tube sealed at both ends and surrounded by a uniform-pressure environment. The fluid inside the sealed tube is in solid-body rotation, and the radial pressure gradient is balanced by the centripetal acceleration: the pressure is highest at the outer radius of the tube and lowest at the centre, and the resulting axial pressure forces at both ends are reacted by the walls. However, if one endwall is removed, the radial distribution of pressure cannot be balanced at the open end: high-pressure fluid near the outer radius of the tube will flow axially outwards to be replaced by external fluid moving inwards along the axis.

Although, as far as the authors are aware, there have been no publications in the scientific literature about self-induced flow in a rotating tube, work has been conducted on related problems. Stewartson (1957) considered the flow inside a cylinder, of length l and radius a, rotating about its polar axis with angular speed Ω. The cylinder was sealed at each end by discs which rotated at an angular speed $\Omega(1-\epsilon)$, where $|\epsilon| \ll 1$. For $E \ll 1$, where $E = \nu/\Omega a^2$ and ν is the kinematic viscosity of the fluid, Stewartson obtained solutions of the linearized equations of motion (in which the nonlinear inertia terms in the Navier–Stokes equations were neglected) and showed that the flow comprises an inviscid core of rotating fluid surrounded by boundary layers on the solid surfaces. Ekman layers (Ekman 1905) with a thickness of order $E^{\frac{1}{2}}$ form on the disks, and shear layers (now referred to as Stewartson layers) form on the cylindrical surface. The Stewartson layers comprise two regions: a layer of thickness of order $E^{\frac{1}{3}}$ in which axial flow occurs, and a layer of thickness of order $E^{\frac{1}{4}}$ in which the angular speed of the core adjusts to that of the cylindrical wall.

Brouwers (1976) considered the case where the disks at each end of the cylinder were porous, and flow was generated by the transfer of fluid through, and/or by the differential rotation of, the disks. He delineated three regimes of flow. In regime (i), for $E^{\frac{1}{3}} \ll G \ll E^{-\frac{1}{2}}$, where $G = l/a$, there is an inviscid core surrounded by Ekman layers and Stewartson layers: the Taylor–Proudman theorem applies in the core where the radial component of velocity is zero, and the axial and tangential components are invariant with the axial distance z. In regime (ii), for $E^{-\frac{1}{2}} \leqslant G \ll E^{-1}$, the tangential component of velocity is sheared from the axis to the cylindrical wall and, although there is still an $E^{\frac{1}{3}}$ layer on this wall and Ekman layers on the disks, the axial component of velocity varies linearly with z. In regime (iii), for $E^{-1} \leqslant G$, viscous effects extend throughout the cylinder, and the flow tends to be restricted to regions near the disks. Although the Brouwers analysis is not of direct relevance to the present problem, there are certain similarities: regimes (i) and (ii) correspond, to some extent, to the short-tube case, and regime (iii) to the long-tube case.

Gilham (1990) extended the linear analysis of Brouwers to the case of a rotating tube, with one end open and the other end sealed, in which the fluid at the open end is in near solid-body rotation. For small values of the Rossby number and large values of G, the flow can be characterized by a single, modified, Ekman number E^*, where $E^* = GE$. For $E^* > 0.2$, recirculation is confined to the open end and the axial component of velocity decays exponentially along the tube; this corresponds to the long-tube case. For $E^* < 0.2$ recirculation occurs throughout the tube and an Ekman layer is formed on the endwall; this corresponds to the short-tube case. For very small values of E^* ($E^* < 0.0025$), the flow is similar to that in Brouwer's regime (i): there is an inviscid core with a Stewartson layer on the cylindrical wall and an Ekman layer on the endwall.

The present paper describes a combined numerical and experimental study of self-induced flow in a rotating tube. The numerical method used to solve the Navier–Stokes equations is outlined in §2, and the experimental apparatus used to

make optical measurements of the velocity and to provide visualization of the flow is described in §3. Comparisons between the computed and experimental results for the flow structure and velocity distribution inside the tube are made in §§4 and 5.

2. Numerical method

2.1. *Equations of motion*

For steady, incompressible, rotationally symmetric, laminar flow, with density ρ and dynamic viscosity μ, the Navier–Stokes and continuity equations can be written (see Schlichting 1979) as

$$\rho\left(u\frac{\partial u}{\partial r}+w\frac{\partial u}{\partial z}-\frac{v^2}{r}\right)=-\frac{\partial p}{\partial r}+\mu\left[\frac{\partial^2 u}{\partial r^2}+\frac{1}{r}\frac{\partial u}{\partial r}+\frac{\partial^2 u}{\partial z^2}-\frac{u}{r^2}\right], \tag{2.1}$$

$$\rho\left(u\frac{\partial v}{\partial r}+w\frac{\partial v}{\partial z}-\frac{uv}{r}\right)=\mu\left[\frac{\partial^2 v}{\partial r^2}+\frac{1}{r}\frac{\partial v}{\partial r}+\frac{\partial^2 v}{\partial z^2}-\frac{v}{r^2}\right], \tag{2.2}$$

$$\rho\left(u\frac{\partial w}{\partial r}+w\frac{\partial w}{\partial z}\right)=-\frac{\partial p}{\partial z}+\mu\left[\frac{\partial^2 w}{\partial r^2}+\frac{1}{r}\frac{\partial w}{\partial r}+\frac{\partial^2 w}{\partial z^2}\right], \tag{2.3}$$

$$\frac{1}{r}\frac{\partial(ru)}{\partial r}+\frac{\partial w}{\partial z}=0, \tag{2.4}$$

where u, v, w are the radial, tangential and axial components of velocity in a stationary, cylindrical-polar coordinate system (r, ϕ, z) and p is the static pressure. As shown in figure 3, the tube, which is open at one end and sealed at the other, is of length l, radius a and rotates with angular speed Ω about its axis; attached to the open end of the tube is an annular disk of outer radius b and inner radius a. The reasons for including the disk are discussed in §2.1.1 below.

2.2. *Boundary conditions*

2.1.1. *The open end*

In the experiments of Ivey (1988), there was a stationary enclosure around the open end of the rotating tube, as described in §3. Gilham (1990) carried out some computations using boundary conditions corresponding to a sealed stationary enclosure, but he found that the problem of computing the flow inside the enclosure could be as difficult as that of computing the flow in the tube itself. The strength of the computed recirculation in the enclosure increased with increasing rotational speed, and the length of the enclosure had to be made impractically large if it were not to affect the flow in the tube.

In a gas-turbine engine, there is an annular rotating disk near the open end of the tube, as shown in figure 1. Ivey measured the axial component of velocity near the sealed end of the rotating tube with and without a disk at the open end, and he found that the disk had only a small effect on the flow. For the computations, it is difficult to specify the boundary conditions in the plane of the open end ($z = 0$, $r < a$) as the flow is recirculating here, but if an annular rotating disk is assumed to be attached to the open end, the problem of specifying the boundary conditions can be simplified. Referring to figure 3, the flow is assumed to enter the system axially through boundary (i), and the flow out of the tube is entrained into the boundary layer on the rotating disk and leaves the system radially through boundary (vi).

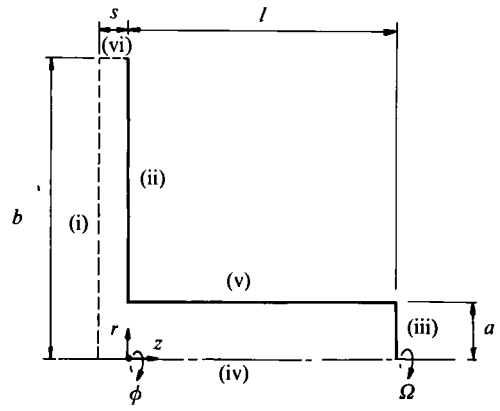

FIGURE 3. Domain of integration for the rotating tube and disk: (i)–(vi) refers to the boundaries.

Conditions near the rotating disk can be specified with some confidence if von Kármán's (1921) equations for the free disk are assumed to apply. The Navier–Stokes equations for an infinite disk rotating in a quiescent fluid are satisfied by similarity solutions of the form:

$$\left.\begin{aligned} &\frac{u}{\Omega r} = F(\zeta), \quad \frac{v}{\Omega r} = G(\zeta), \quad \frac{w}{(\Omega\nu)^{\frac{1}{2}}} = H(\zeta), \quad \frac{p}{\rho\Omega\nu} = -P(\zeta), \\ &\text{where} \qquad \zeta = z'\left(\frac{\Omega}{\nu}\right)^{\frac{1}{2}}. \end{aligned}\right\} \tag{2.5}$$

Here $z' = -z$ is the axial distance from the disk, ν is the kinematic viscosity, and $F(\zeta)$, $G(\zeta)$, $H(\zeta)$ are functions that satisfy the boundary conditions:

$$\left.\begin{aligned} &F(0) = 0, \quad G(0) = 1, \quad H(0) = 0, \\ &F(\zeta) \to 0, \quad G(\zeta) \to 0 \quad \text{as} \quad \zeta \to \infty. \end{aligned}\right\} \tag{2.6}$$

Cochran (1934) obtained the first numerical solutions of the von Kármán equations and, in particular, found that $H(\zeta) \to 0.886$ as $\zeta \to \infty$. Recently, Rogers (see Owen & Rogers 1989) obtained more accurate solutions which agree with Cochran's values except for the limiting value of $H(\zeta)$, which was found to be 0.8845; the solutions of Rogers are identical to those of Benton (1966).

It is convenient to define the edge of the boundary layer on the free disk as the point where $v/\Omega r = 0.01$; using this definition, the boundary-layer thickness, δ, is given by

$$\delta \approx 5.5\left(\frac{\nu}{\Omega}\right)^{\frac{1}{2}}. \tag{2.7}$$

For the computations described below, it is assumed that the free-disk boundary conditions are appropriate for a finite annular disk rotating in a quiescent fluid of finite extent. Boundary (i), shown in figure 3, is assumed to be far enough away from the disk for the conditions at infinity to apply, such that, at $z = -s$,

$$u = 0, \quad v = 0, \quad p = p_a, \tag{2.8}$$

where p_a is the constant atmospheric pressure. For boundary (vi), it is assumed that

the radius b of the disk is large enough for the similarity conditions given in (2.5) to apply, such that, at $r = b$,

$$\frac{\partial}{\partial r}\left(\frac{u}{r}\right) = 0, \quad \frac{\partial}{\partial r}\left(\frac{v}{r}\right) = 0, \quad \frac{\partial w}{\partial r} = 0, \quad \frac{\partial p}{\partial r} = 0. \tag{2.9}$$

These two conditions ensure that, as for the free disk, fluid enters the system axially through boundary (i) and leaves radially through boundary (vi).

For the computations described below, the radius of the disk was set arbitrarily as $b = 5a$. For most cases, the axial limit of the integration domain was set as $s = a$: this ensured that $\delta \ll s$. In some cases, s was increased on an *ad hoc* basis to ensure that the flow inside the tube was not affected significantly by the boundary conditions at the open end. (For the case of a solid disk, Gilham 1990 found that a value of $s = 4\delta$ was sufficient to ensure that the computed velocity profiles were in good agreement with the free-disk results of Rogers.)

2.2.2. *Conditions for the six boundaries*

As stated above, the conditions for boundaries (i) and (vi) shown in figure 3 were based on the free-disk boundary conditions. Symmetry conditions were used for boundary (iv), and no-slip conditions were used for the other boundaries. For completeness, all six boundary conditions are written below.

$$\left.\begin{array}{lllllll}
\text{(i)} & z = -s, & 0 \leqslant r \leqslant b: & u = 0, & v = 0, & p = p_{\mathrm{a}}; & \\
\text{(ii)} & z = 0, & a \leqslant r \leqslant b: & u = 0, & v = \Omega r, & w = 0; & \\
\text{(iii)} & z = l, & 0 \leqslant r \leqslant a: & u = 0, & v = \Omega r, & w = 0; & \\
\text{(iv)} & r = 0, & -s \leqslant z \leqslant l: & u = 0, & v = 0, & \dfrac{\partial w}{\partial r} = 0; & \\
\text{(v)} & r = a, & 0 \leqslant z \leqslant l: & u = 0, & v = \Omega a, & w = 0; & \\
\text{(vi)} & r = b, & -s \leqslant z \leqslant 0: & \dfrac{\partial}{\partial r}\left(\dfrac{u}{r}\right) = 0, & \dfrac{\partial}{\partial r}\left(\dfrac{v}{r}\right) = 0, & \dfrac{\partial w}{\partial r} = 0, & \dfrac{\partial p}{\partial r} = 0.
\end{array}\right\} \tag{2.10}$$

2.3. *Numerical solution*

Numerical integration of the governing equations (2.1)–(2.4) with boundary conditions (2.10) was achieved with a finite-difference algorithm incorporating a multigrid acceleration technique (see Vaughan, Gilham & Chew 1989). Finite-difference replacements were made for the governing equations using a non-uniform rectangular staggered grid covering the integration domain, and the resulting difference equations were solved using a V-cycle nonlinear multigrid method incorporating the SIMPLEC pressure-correction scheme of van Doormaal & Raithby (1984). Further details are given below, and the interested reader is referred to Gilham (1990).

2.3.1. *Finite-difference equations*

The finite-difference equations were obtained by integration of the momentum equations, in the manner detailed by Patankar (1980), over the control volumes formed by a rectangular non-uniform staggered grid covering the domain. The grid was of the form recommended by Patankar & Spalding (1972) in which the control volumes for the radial and axial components of velocity (the u-cell and w-cell

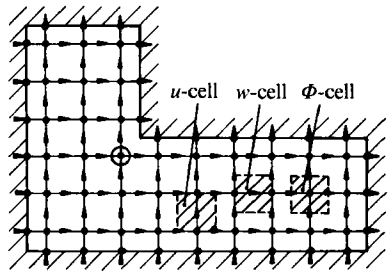

FIGURE 4. Finite-difference grid used in the computation.

respectively) are shifted or staggered such that they lie midway between the control volumes at which the tangential component of velocity and pressure are calculated (the Φ-cell). The grids were generated by expanding and contracting the spacing of the Φ-cell nodes in accordance with a geometric progression. Typically, 65 radial and 128 axial nodes were used within the tube, and 97 radial and 65 axial nodes in the region surrounding the open end. A simplified example of the finite-difference grid is shown in figure 4.

The momentum equations can be expressed in the common form

$$\frac{1}{r}\frac{\partial}{\partial r}(\rho r u\Phi)+\frac{\partial}{\partial z}(\rho w\Phi)=\frac{1}{r}\frac{\partial}{\partial r}\left(\mu r\frac{\partial\Phi}{\partial r}\right)+\frac{\partial}{\partial z}\left(\mu\frac{\partial\Phi}{\partial z}\right)+S_{\Phi}, \tag{2.11}$$

where Φ represents the generalized variable (u, v, w) and S_{Φ} is a source term. Integration of (2.11) over the control volumes (see Patankar 1980) leads to the finite-difference equation:

$$A_{p,\Phi}\Phi_{\mathrm{p}}=\Sigma_{\mathrm{nb}}A_{\mathrm{nb},\Phi}\Phi_{\mathrm{nb}}+S_{1,\Phi}+S_{2,\Phi}\Phi_{\mathrm{p}}. \tag{2.12}$$

Here Σ_{nb} represents the summation of the coefficients over the four neighbouring nodes, Φ_{nb} the values of Φ at these nodes, $S_{1,\Phi}$ and $S_{2,\Phi}$ are the coefficients of the linearized source term, and $A_{\mathrm{p},\Phi}$ and $A_{\mathrm{nb},\Phi}$ are coefficients resulting from the control-volume integration. Further details are given by Gilham (1990).

The continuity equation was used to devise a pressure-correction equation in the manner described by van Doormaal & Raithby (1984). This equation, which had the dual role of determining the pressure and ensuring that the velocity field satisfied continuity, has the same form as (2.12).

Boundary conditions were introduced via the boundary nodes, and for Neumann conditions a second-order central or backward difference was used to set the boundary value. When the pressure was specified, the pressure correction was set to zero, implying continuity in the boundary cells. Thus, only one of the axial and radial velocities was prescribed, and the other was found by rewriting the continuity equation as a flux condition. Starting values were obtained by setting all variables to zero.

2.3.2. *Multigrid algorithm*

The coupled system of nonlinear equations given in §2.3.1 was solved using a V-cycle nonlinear multigrid algorithm, as described by Vaughan *et al.* (1989). In multigrid methods, which employ a series of progressively coarser grids, the finite-difference equations are 'relaxed' (i.e. partially solved) on a fine grid, initially the

finest grid. Following relaxation, the residuals of the equations are evaluated, and both the residuals and the current solution are 'restricted' (i.e. transferred) to a coarser grid using a restriction operator.

The processes of relaxation and restriction are repeated until the coarsest grid is reached, after which a process of relaxation followed by 'prolongation' (i.e. interpolation) is undertaken in which the coarse-grid equations are relaxed and corrections for the finer grid evaluated. These corrections are then prolongated to the finer grid and the solution updated. These processes of relaxation and prolongation are repeated until the finest grid is reached, where the updated solution forms an improved fine-grid solution. The above cycle from fine to coarse to fine grid (commonly referred to as a V-cycle) is repeated until convergence is achieved.

The relaxation process used here was the SIMPLEC pressure-correction scheme of van Doormaal & Raithby. The finite-difference momentum equations were solved using one alternating-line Gauss–Seidel relaxation sweep, and the pressure-correction equation was solved using six sweeps. Following relaxation, the velocities and pressure were corrected. On the finest and intermediate grid levels, the process of smoothing and correction was repeated once, and on the coarsest grid twice, to ensure a sufficiently smooth solution.

Under-relaxation was required owing to the nonlinearity of the equations. It was implemented implicitly, via the coefficients, for the momentum equations, and explicitly for the pressure. The under-relaxation factors for the momentum equation were typically 0.3, and for the pressure 0.5, although these values were changed for different Ekman numbers. The strong coupling between the radial and tangential momentum equations, and the dominance of the centripetal-acceleration term ($\rho v^2/r$) within the radial momentum equation necessitated additional under-relaxation. This was achieved by using the distributive damping terms suggested by Gosman *et al.* (1976): $\alpha_G\, \rho|v|/r(u^{n-1}-u^n)$, where the superscripts $n-1$ and n refer to successive iterations, was added to the source term of the radial momentum equation; a value of $\alpha_G \approx 50$ was found to be satisfactory.

The coarse grids were generated by omitting alternate Φ-cell nodes in both directions, with the u-cells and w-cells being staggered halfway between. A nine-point grid-weighted restriction operator for the Φ-cells, and a six-point operator for the u-cells and w-cells were used to transfer the variables and residuals from the fine to the coarse grids. For most of the results presented below, three grid levels were used, and prolongation of the correction from the coarse to fine grids was made using bilinear interpolation.

The root-mean-square residual, RMS_Φ, was defined as

$$\mathrm{RMS}_\Phi = [\textstyle\sum_{ij}(\Phi^n-\Phi^{n-1})^2/\sum_{ij}(\Phi^n)^2]^{\frac{1}{2}},$$

where Φ^n and Φ^{n-1} represent the current and previous iterative values, respectively, and Σ_{ij} indicates summation over all grid nodes. Convergence was said to have occurred when RMS_Φ dropped below a specified value (typically 10^{-5}). Additional checks, involving overall balances in conserved quantities such as mass and momentum, were also used to ensure convergence.

The numerical method was validated by comparing the computed velocities with available 'exact solutions', such as Rogers' results for the free disk (see Owen & Rogers 1989), and with experimental data for related problems, like vortex breakdown in a sealed rotor-stator system (see Escudier 1984). Details of these validation tests, for which good results were achieved, are given by Gilham (1990).

For the rotating-tube problem considered here, computations were conducted for $5 \leqslant G \leqslant 40$ and $5 \times 10^{-5} \leqslant E \leqslant 0.04$. The number of finite-difference nodes used, and the computational time taken, depended on the values of G and E. For example, for $G = 10$ and $E = 0.002$, with 128 axial and 65 radial nodes in the tube, and 65 axial and 97 radial nodes in the open-end region near the disk, the multigrid method required 89 iterations to obtain a converged solution ($\mathrm{RMS}_\phi < 10^{-5}$ for all variables); on a VAX 8530 computer, this took 672 minutes of CPU time. Whilst this represents a considerable amount of computing time, the equivalent single-grid solution required 4615 iterations and took 3578 minutes of CPU time!

3. Experimental apparatus

Figure 5 shows the rotating-tube rig used for the optical measurements. A horizontal glass tube, with one end partially enclosed by a stationary casing that was open to the atmosphere and the other end sealed by a Perspex disk, was supported on ball-bearing assemblies, which themselves were attached to a baseplate. The tube was rotated at speeds up to 6000 rev/min. by an electric motor and belt-drive, and the rotational speed was measured to an accuracy of 1% by an electronic tachometer.

Velocity measurements inside the tube were obtained by laser–Doppler anemometry (LDA) operating in the forward-scatter real-fringe mode, and micron-size silicone oil particles were used to 'seed' the air outside the stationary enclosure at the open end of the tube. A 15 mW Spectra-Physics He–Ne laser was used as the light source, and a Malvern Instruments beam-splitter and frequency-shift unit were employed in the transmitting optics. The beam separation at transmission was 20 mm and the focal length of the transmitting lens was 150 mm, which resulted in a probe volume approximately 110 μm diameter and 1.7 mm length with a fringe spacing of 4.75 μm. The receiving optics included an F1.8 lens of 50 mm focal length, a 50 μm pinhole and an EMI photomultiplier, and the resulting signal (with Doppler frequencies mainly in the range 30–100 kHz) was processed by a Cambridge Consultants tracking filter used in the frequency counting mode. In this mode of operation the instrument was accurate to $\mp 0.1\%$.

Uncertainty in the measured velocity was caused by radial and angular misalignment of the probe volume, refraction in the glass tube, velocity biasing due to the size of the probe volume, and round-off errors in the measured frequencies. Of these, the uncertainty caused by angular misalignment was considered to be the largest. For example, when measuring the axial component of velocity near the outer radius of the tube (where the axial component is much smaller than the tangential one), a small angular misalignment can cause a small fraction of the large tangential component of velocity to be added to the signal. As shown by Ivey (1988), an angular misalignment of only 0.25° was found to give large errors in w near the outer part of the tube. Measurements of the tangential component of velocity were validated by sealing the tube to ensure solid-body rotation; no such validation of the axial component was possible. However, despite all the problems, most of the results presented below were in good agreement with the computed velocities.

For flow visualization, a 4W Spectra Physics argon-ion laser, a cylindrical lens and a bi-convex lens were used to produce a collimated sheet of light which entered the tube at the open end. The light sheet was parallel to, and coincident with, the axis of the tube and, to reduce flare, the width of the light sheet was slightly less than the diameter of the tube. A Concept smoke generator, which could be pulsed, released

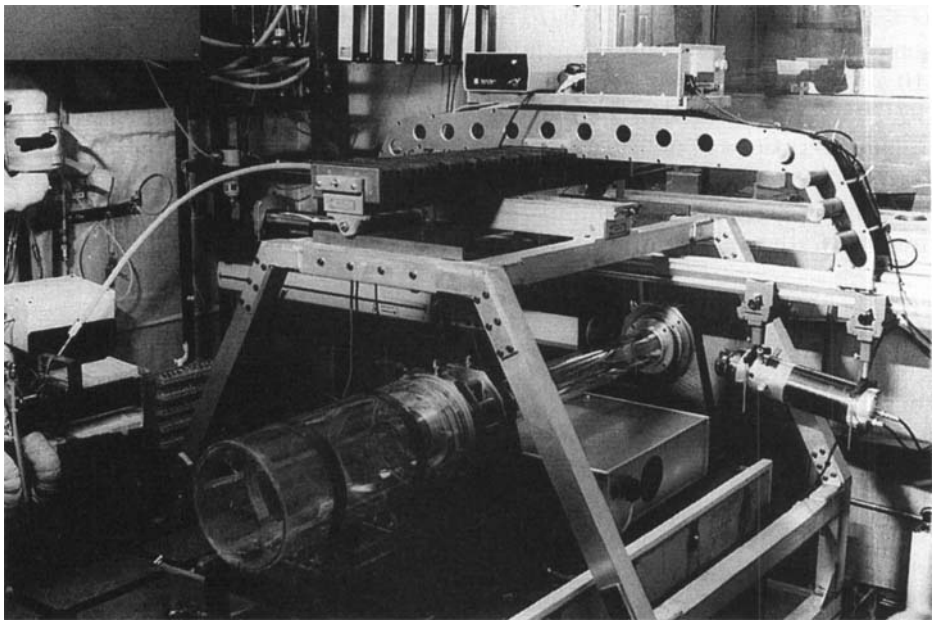

FIGURE 5. Rotating-tube rig used for the optical measurements. (Stationary enclosure is at left-hand end of glass tube. Laser transmitting optics are to left of tube; receiving optics to right.)

clouds of micron-sized oil particles into the air surrounding the open end of the tube. Photographs were obtained with a Canon A1 camera, operating in the 'aperture-preferred mode' at F1.4, using ISO 400 black and white film.

Further details of the rig and instrumentation are given by Ivey (1988).

4. Flow structure

4.1. *Flow visualization*

Figures 6 and 7 show photographs taken near the open end and the sealed end, respectively, of the rotating tube. The length and radius of the tube were $l = 1050$ mm and $a = 36.5$ mm ($G = 28.8$), and the rotational speed was 175 rev/min. ($E = 6.25 \times 10^{-4}$). A pulse of smoke was released into the enclosure at the open end, an (r, z) plane was illuminated by the argon-ion laser, and photographs were taken at five frames per second. The datum $t = 0$ refers to the time, after smoke had entered the tube, when the first photograph was taken, and subsequent times refer to this datum.

In figure 6, the open end is at the left and the start of a bearing assembly, at $z/l = 0.38$, can be seen at the right. The smoke, which appears white in the photographs, moves progressively along the centre of the tube and reaches the bearing at $t \approx 1$ s. For $t \geqslant 1.2$ s, the boundary between the central core of smoke, flowing towards the sealed end, and the clear returning air (which appears black) can be readily seen.

In figure 7, the smoke front has moved past the second bearing assembly, which ends at $z/l = 0.62$, and reaches the sealed end at $t \approx 3.6$ s. For $t \geqslant 4.2$ s, the smoke flows radially outward in the boundary layer on the disk at the sealed end, and

(*a*) $t = 0$ s

(*b*) $t = 0.2$ s

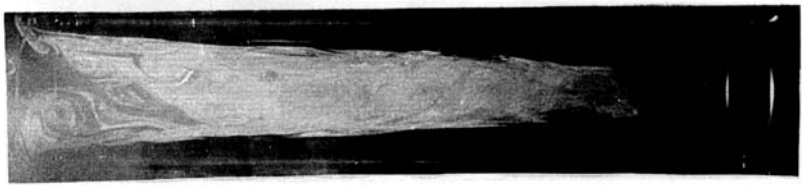

(*c*) $t = 1.0$ s

(*d*) $t = 1.2$ s

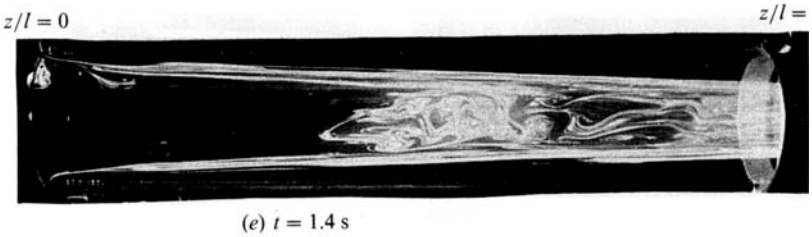

(*e*) $t = 1.4$ s

FIGURE 6. Flow visualization near the open end of the tube. $G = 28.8$, $E = 6.25 \times 10^{-4}$.

returns towards the open end in an annular boundary layer on the cylindrical wall of the tube. Flare from the solid surfaces, particularly from the disk, makes flow visualization difficult near the sealed end, and careful inspection of the photographs is necessary.

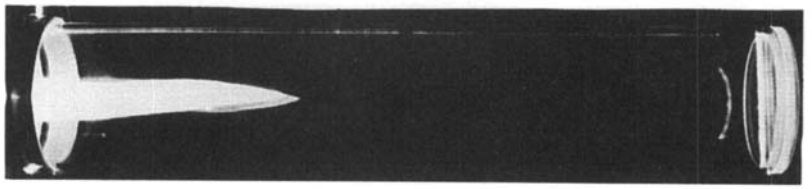

(a) $t = 2.0$ s

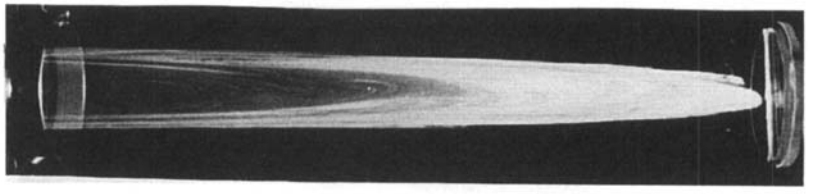

(b) $t = 3.6$ s

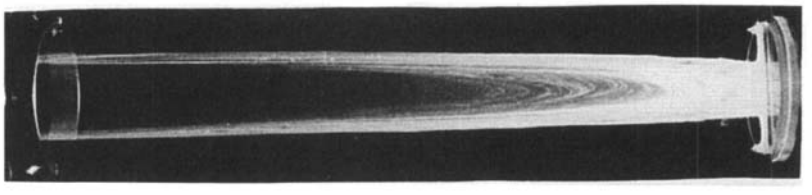

(c) $t = 4.2$ s

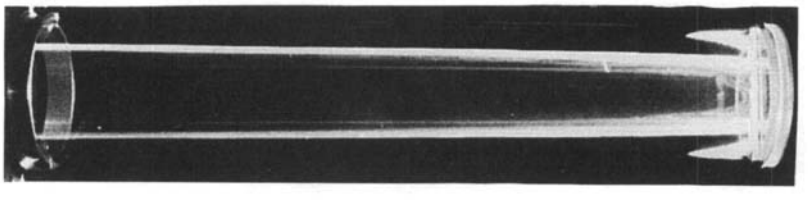

(d) $t = 5.0$ s

$z/l = 0.62$ $z/l = 1.0$

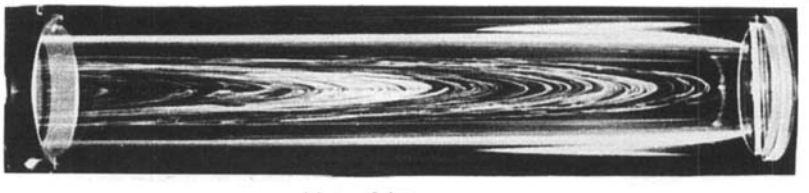

(e) $t = 6.4$ s

FIGURE 7. Flow visualization near the sealed end of the tube. $G = 28.8$, $E = 6.25 \times 10^{-4}$.

In some of the earlier tests of Owen & Pincombe (1981), self-induced flow was observed in a rotating tube with no endwalls. In principle, with identical conditions at each end of the tube, the flow should be symmetrical about the mid-axial plane, $z/l = 0.5$. In practice, the flow is unstable to small disturbances, and there is a

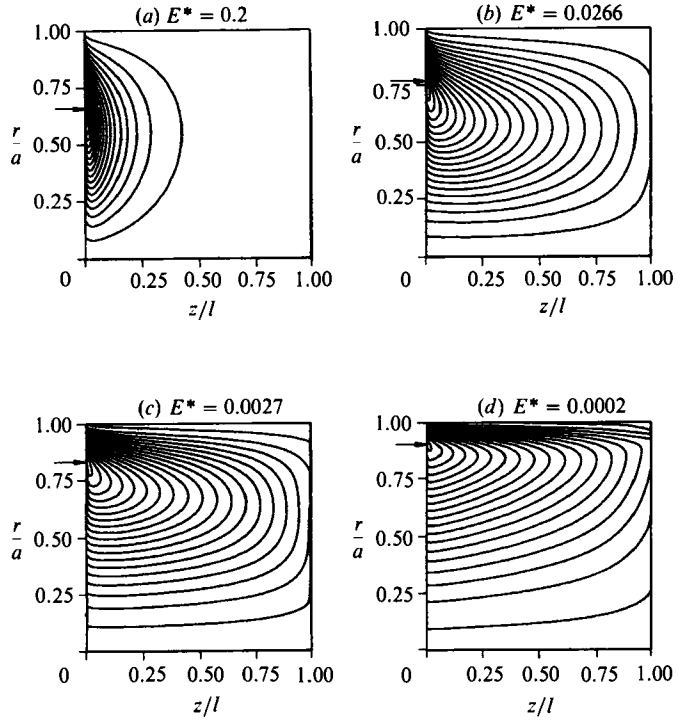

FIGURE 8. Computed streamlines for $G \approx 40$. The arrows show the boundary between axial inflow and outflow.

'preferred' direction. However, the fact that self-induced flow still occurs inside a tube with no endwall serves to illustrate the point, which is reinforced by the results presented below, that the flow in a long rotating tube is generated principally by the *cylindrical* wall of the tube.

4.2. *Computed streamlines*

The stream function, Ψ, where

$$u = \frac{1}{r}\frac{\partial \Psi}{\partial z}, \quad w = -\frac{1}{r}\frac{\partial \Psi}{\partial r}, \tag{4.1}$$

was obtained by integrating the computed velocity distributions. It is useful to present the computed velocities and 'streamlines' (or plots of constant Ψ) in terms of a modified Ekman number, E^*, where

$$E^* = GE = \frac{\nu l}{\Omega a^3}. \tag{4.2}$$

As stated in §1, Gilham (1990) obtained solutions of the linear equations and showed that for $G \gg 1$ the flow could be uniquely characterized by E^*: it is unnecessary to specify G and E separately. In §5, it is demonstrated that E^* can also be used to characterize the flow even when the Navier–Stokes equations, rather than the linear equations, are solved.

Figure 8 shows the computed streamlines for $G \approx 40$. (The discontinuities in the streamlines shown in the figures at $z/l = 1$ are caused by the fact that, for the scale

used, the thickness of the Ekman layer is negligible.) In figure 8(*a*), for $E^* = 0.2$, which corresponds to the long-tube case, circulation is restricted to a region near the open end at $z/l = 0$. For $E^* < 0.2$, which corresponds to the short-tube case, figures 8(*b–d*) shows that progressively more flow reaches the sealed end ($z/l = 1$) as E^* is reduced. In figure 8(*d*) there are indications of boundary layers on the cylindrical wall, at $r/a = 1$, and on the disk at the sealed end. It can also be seen that only a fraction of the fluid entering the tube reaches the sealed end: most is recirculated from the core into the annular boundary layer on the cylindrical wall. (This recirculation is not readily apparent in figures 6 and 7, which were photographed at $E^* = 0.018$, as most of the fluid in the boundary layers on the cylindrical wall was entrained from regions into which the smoke had not been convected.)

5. Velocity distributions

5.1. *Axial variations of velocity along the tube*

Figure 9 shows the effect of G on the computed axial variation of $w/\Omega a$ along the axis of the tube. Figure 9(*a*), for $E^* = 0.2$, corresponds to the long-tube case in which, away from the open end, the velocity decays rapidly with axial distance. Figure 9(*b*), for $E^* = 0.002$, corresponds to the short-tube case in which, away from the boundary layer on the endwall, the decay of velocity is more gradual. In both cases, for $G \geqslant 20$ the effect of G is relatively weak and the velocity distribution depends mainly on E^*; this is consistent with Gilham's (1990) solution of the linear equations, referred to in §1, in which for $G \gg 1$ the flow depends solely on E^*. For comparison with experimental data, the results presented below were all obtained for $G = 42.6$.

The effects of E^* on the axial variation of the axial and tangential components of velocity are shown in figure 10. Figure 10(*a*) provides a comparison between the computed values of $w/\Omega a$, on the tube axis, and the velocities measured for $E^* = 0.0266$ and 0.0027 by the LDA system described in §3. It should be remembered that the experiments were conducted using a stationary enclosure at the open end whereas the numerical model used a rotating disk. However, away from the open end, agreement between the computed and measured velocities is very good, and both sets of results converge near the boundary layer on the endwall. (As stated in §2.2.1, the measurements of Ivey (1988) suggested that a rotating disk has only a small effect on the flow near the sealed end.)

It can be seen from figure 10(*a*) that for $E^* \leqslant 0.0266$, where short-tube conditions prevail, $w/\Omega a$ decreases as E^* decreases; however, as $E^* \propto (\Omega a)^{-1}$, w itself increases as E^* decreases. It can also be seen that the axial decay of $w/\Omega a$ is attenuated as E^* decreases.

Additional insight can be gained by considering the axial variation of the tangential components of velocity shown in figure 10(*b*). The distributions of $v/\Omega r$, which were computed at $r/a = 0.017$, show a monotonic decrease of the magnitude of $v/\Omega r$ with decreasing E^*. For $E^* = 0.2$, the fluid is virtually in solid-body rotation ($v/\Omega r = 1$) for $z/l > 0.6$; for $E^* = 0.0002$, there is very little rotation of the fluid in the core outside the boundary layer on the endwall.

5.2. *Radial variation of velocity near the open and sealed ends*

Figure 11 shows the effect of E^* on the radial variation of $w/\Omega a$. In figure 11(*a*), near the open end at $z/l = 0.129$, there is mainly good agreement between the computed and measured velocities for $E^* = 0.0266$ and 0.0027. It can be seen that, as shown in §4, there is a central core of fluid moving towards the sealed end ($w > 0$), with fluid

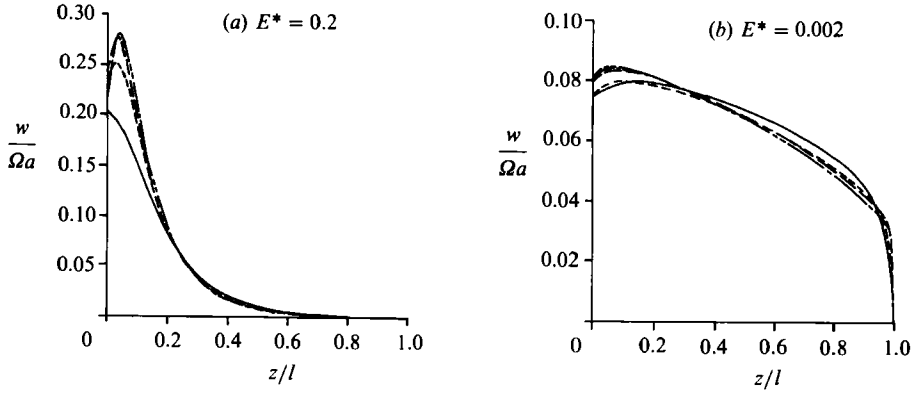

FIGURE 9. Effect of G on the computed axial variation of the axial component of velocity along the axis of the tube. —, $G = 5$; ----, $G = 10$; —, $G = 20$; ---, $G = 30$; ----, $G = 40$.

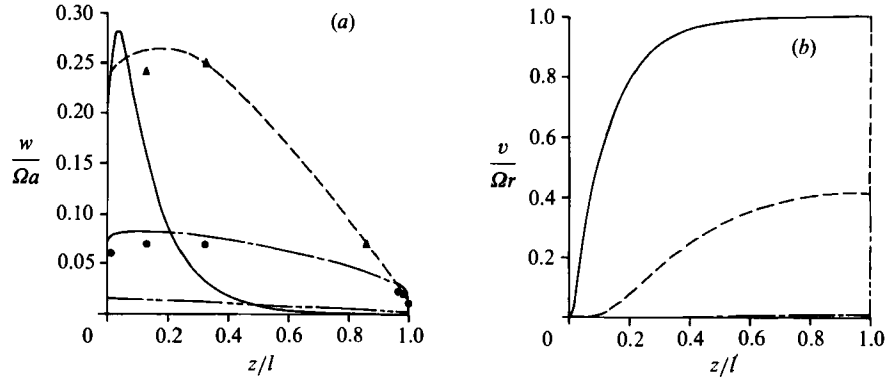

FIGURE 10. Effect of E^* on the axial variation of the velocity for $G \approx 40$. (*a*) $w/\Omega a$ at $r/a = 0$; (*b*) $v/\Omega r$ at $r/a = 0.017$. Numerical solutions: —, $E^* = 0.2$; ---, $E^* = 0.0266$; —, E^* 0.0027; ----, $E^* = 0.0002$. Experimental data: ▲, $E^* = 0.0266$; ●, $E^* = 0.0027$.

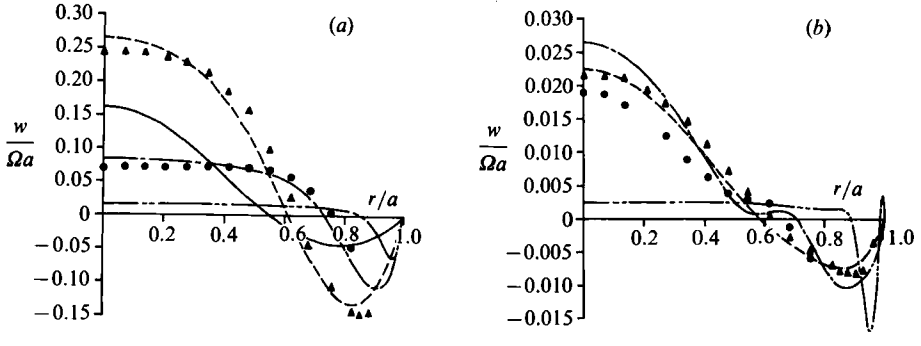

FIGURE 11. Effect of E^* on the radial variation of the axial component of the velocity for $G \approx 40$. (*a*) at $z/l = 0.129$; (*b*) at $z/l = 0.984$. Numerical solutions: —, $E^* = 0.2$; ----, $E^* = 0.0266$; —, $E^* = 0.0027$; ---- $E^* = 0.0002$. Experimental data: ▲, $E^* = 0.0266$; ●, $E^* = 0.0027$.

returning in an annular boundary layer ($w < 0$). For short-tube conditions ($E^* < 0.2$), the magnitude of $w/\Omega a$ (but not necessarily the magnitude of w) and the thickness of the annular layer decreases as E^* decreases; in the central core, the velocity distribution becomes flatter as E^* decreases.

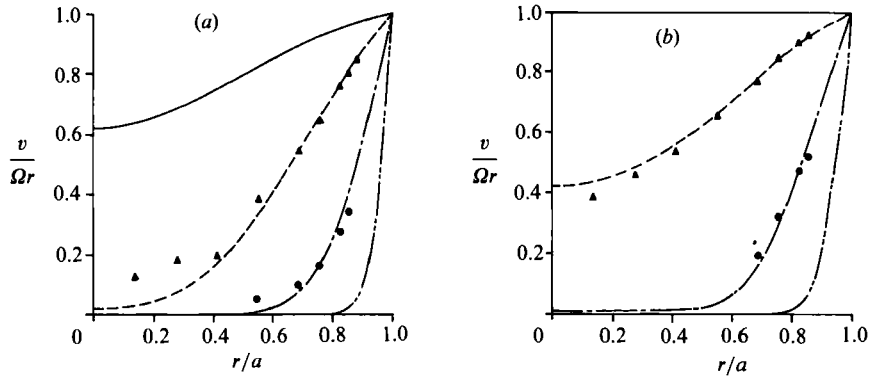

FIGURE 12. Effect of E^* on the radial variation of the tangential component of the velocity for $G \approx 40$. (*a*) at $z/l = 0.129$; (*b*) at $z/l = 0.984$. Numerical solutions: —, $E^* = 0.2$; – –, $E^* = 0.0266$; – – –, $E^* = 0.0027$; – – – –, $E^* = 0.0002$. Experimental data: ▲, $E^* = 0.0266$; ●, $E^* = 0.0027$.

In figure 11 (*b*), near the sealed end at $z/l = 0.984$, the agreement between the measured and computed velocities for $E^* = 0.0266$ and 0.0027 is not as good as at the open end. However, it should be noted that the scale for $w/\Omega a$ in figure 11 (*b*) is an order of magnitude different from that in figure 11 (*a*). It should also be pointed out that the positional uncertainty in the axial location of the probe volume was $\mp$ 0.25 mm: referring to figure 9 (*b*), it can be seen that a small variation in z/l can cause a large variation in $w/\Omega a$ at $z/l = 0.984$. Despite these difficulties, both measured and computed velocities show similar trends: the inflexion at $r/a \approx 0.6$ for $E^* = 0.0027$ is caused by the boundary layer on the endwall, which is discussed in §5.3. (The region near $r/a = 1$ where $w > 0$ for $E^* = 0.0002$ is a small recirculation zone formed by the radially outward flow in the boundary layer on the disk meeting the axial flow in the boundary layer on the cylindrical wall.) By comparing figure 11 (*b*) with 11 (*a*), it can be seen that, for $E^* = 0.0266$ and 0.0027, the thickness of the annular boundary layer increases with increasing z/l; for $E^* = 0.0002$, the thickness of this layer is almost invariant with z; for $E^* = 0.2$, $w = 0$ near the sealed end.

Figure 12 shows the effect of E^* on the radial variation of $v/\Omega r$ near the open and sealed ends of the tube; the conditions correspond to those for figure 11. The agreement between the computed and measured velocities for $E^* = 0.0266$ and 0.0027 is mainly good except, for $z/l = 0.129$, near the tube axis. It can be seen that, for a fixed radial location, $v/\Omega r$ decreases as E^* decreases and increases as z/l increases. For $E^* = 0.2$, the fluid is in solid-body rotation near the sealed end; for $E^* = 0.0002$, there is no significant rotation in the central core even near the sealed end.

The three regimes of Brouwers, discussed in §1, have characteristics that can be observed in figures 11 and 12. The velocity distributions for $E^* = 0.0002$ behave like those in regime (i): the layers in which $w < 0$ and $v > 0$ correspond, qualitatively at least, to the $E^{\frac{1}{3}}$ and $E^{\frac{1}{4}}$ Stewartson layers. The distributions for $E^* = 0.0266$ are consistent with regime (ii), in which the tangential component of velocity is sheared from the axis to the wall. For $E^* = 0.2$, the flow is restricted to a region near the inlet in a manner similar to that for regime (iii).

It is worth pointing out that the overall agreement between the measured and computed values implies (as was presumed in §2) that the flow remains laminar for values of E^* as low as 0.0027 and of E as low as 5×10^{-5}. As these values are quite typical of those found inside the anti-icing tubes of aero engines, it implies that the self-induced-flow problem is one of the few examples of laminar flow occurring inside

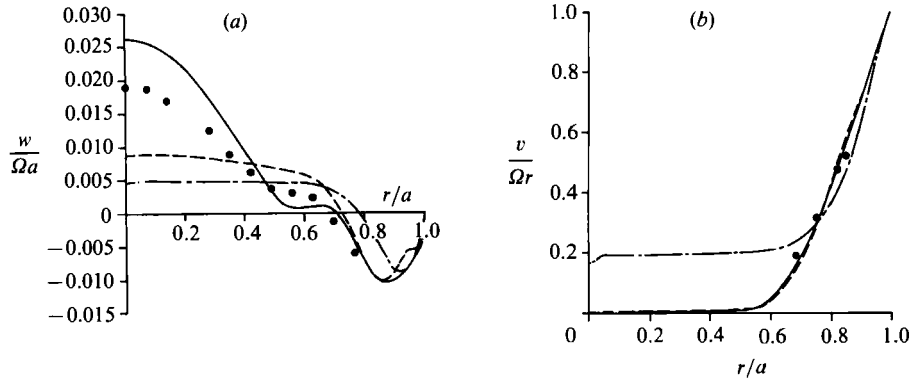

FIGURE 13. Effect of ζ on the velocity distributions at the sealed end for $G = 42.6$, $E^* = 0.0027$. (*a*) Radial variation of $w/\Omega a$; (*b*) radial variation of $v/\Omega r$. Numerical solutions: —, $\zeta = 86$; ----, $\zeta = 5.5$; – –, $\zeta = 2$. Experimental data: ●, $\zeta = 86$.

jet engines! The authors are unaware of a suitable criterion that can be used to estimate the transition from laminar to turbulent self-induced flow.

5.3. *Distribution of velocity in the boundary layer on the endwall*

It is shown below that the flow in the boundary layer on the endwall is similar to that for the free disk discussed in §2.1.1. It is appropriate, therefore, to use the non-dimensional axial coordinate $\zeta = z' (\Omega/\nu)^{\frac{1}{2}}$, where z' is the axial distance from the disk at the sealed end. Here, $z' = l - z$; in equation (2.5), the axial distance from the disk at the open end of the tube was taken as $z' = -z$. Although the flow in the tube, outside the boundary layer on the endwall, is governed by the modified Ekman number, E^*, the flow in the boundary layer itself is controlled mainly by the conventional Ekman number, E.

Figure 13 shows radial variations of $w/\Omega a$ and $v/\Omega r$ for $G = 42.6$ and $E = 6.25 \times 10^{-5}$ ($E^* = 0.0027$) and for $\zeta = 2$, 5.5 and 86. The experimental data for $\zeta = 86$ correspond to those shown in figures 11(*b*) and 12(*b*) for $z/l = 0.984$ and $E^* = 0.0027$.

Figure 13(*a*) shows that, as ζ is reduced, the distribution of $w/\Omega a$ in the central core changes from the shape associated with flow in the tube to a flat distribution associated with flow in the boundary layer on the free disk, where w is invariant with r. Similarly, figure 13(*b*) shows that the core rotation is insignificant for $\zeta \leqslant 5.5$, which is close to the approximate edge of the boundary layer, as given by (2.7). It appears, therefore, that the central part of the endwall, for $r/a \leqslant 0.6$, behaves like the free disk.

This free-disk behaviour is shown more clearly in figure 14. It should be pointed out that, to ensure accurate computations, 32 finite-difference nodes were used in the axial region $0 \leqslant \zeta \leqslant 10$, and 65 nodes were used across the radius of the disk. The computed values of $u/\Omega r$, $v/\Omega r$ and $w/(\Omega\nu)^{\frac{1}{2}}$ are compared with the free-disk distributions of Rogers (see Owen & Rogers 1989) for $r/a = 0.25$, 0.50 and 0.75.

For small values of ζ, the computed values of $u/\Omega r$ in figure 14(*a*) are similar to the free-disk distributions. As ζ increases, the differences become larger; the negative values of $u/\Omega r$ for $r/a = 0.75$ are associated with the spatially oscillating flow that occurs near a rotating disk in a rotating fluid (see Owen & Rogers).

For $r/a \leqslant 0.50$, the computed values of $v/\Omega r$ in figure 14(*b*) are virtually indistinguishable from the free-disk distributions. For $r/a = 0.75$ and for the larger values of ζ, there is evidence of the core rotation that causes the oscillatory flow

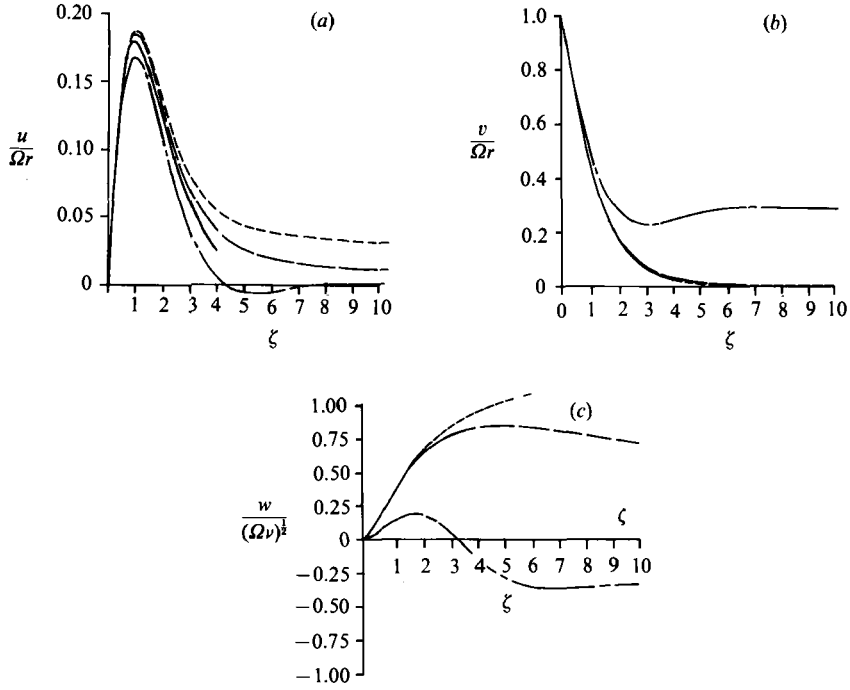

FIGURE 14. Effect of r/a on the axial velocity distributions at the sealed end for $G = 42.6$, $E^* = 0.0027$. (a) Axial variation of $u/\Omega r$; (b) axial variation of $v/\Omega r$; (c) axial variation of $w/(\Omega\nu)^{\frac{1}{2}}$. Numerical solutions: ----; $r/a = 0.25$; —, $r/a = 0.50$; –·–, $r/a = 0.75$. Free-disk profiles: —, Rogers (see Owen & Rogers 1989).

referred to above. In figure 14(c), for $r/a \leqslant 0.5$ and for the smaller values of ζ, the computed values of $w/(\Omega\nu)^{\frac{1}{2}}$ are similar to the free-disk distributions; for the larger values of ζ, the computed axial components of velocity approach those associated with the flow in the core of the tube. The distribution of $w/(\Omega\nu)^{\frac{1}{2}}$ for $r/a = 0.75$ demonstrates the recirculation that occurs near the corner, at $r/a = 1$ and $z/l = 1$, as the fluid leaves the boundary layer on the disk to return in the annular layer on the cylindrical wall of the tube.

For a constant value of E, the radial extent over which free-disk-type flow occurs will increase if G is reduced. However, as pointed out in §4.2, only a fraction of the fluid entering the tube reaches the sealed end: most of the 'pumping effect' created by the rotating tube is caused by entrainment into the boundary layer on the cylindrical wall rather than into the boundary layer on the end disk.

6. Conclusions

When a tube, open at one end and sealed at the other, rotates about its axis, fluid flows from the open end along the axis towards the sealed end and returns in an annular boundary layer on the cylindrical wall. This self-induced flow, which can occur under isothermal condition, is believed to be responsible for the so-called 'hot-poker effect' used to provide anti-icing protection for the nose bullets of some jet engines.

Experimental measurements have been obtained using flow visualization and LDA in a transparent rotating-tube, and numerical solutions of the Navier–Stokes equations have been computed using a finite-difference multigrid technique. Despite

the experimental difficulties, and despite the fact that the conditions at the open end of the experimental rig were different from those assumed for the numerical solutions, the agreement between the measured and computed velocity distributions was mainly good.

In general, the flow in the tube is governed by the length-to-radius ratio, G, and the Ekman number, E. However, for sufficiently large values of G (typically, $G \geqslant 20$) the flow outside the boundary layer on the endwall can be characterized by the single non-dimensional group, E^*, a modified Ekman number where $E^* = GE$.

Most, or sometimes all, of the fluid entering the open end of the tube is entrained into the annular (Stewartson-type) boundary layer before it reaches the sealed end, and the axial component of velocity on the axis of the tube decays with distance from the open end. For small values of E^* ($E^* < 0.2$), some of the flow reaches the sealed end: this is called the short-tube case, which can be used for anti-icing nose bullets. For larger values of E^* ($E^* \geqslant 0.2$), the axial component of velocity decays to zero before the sealed end is reached: this is called the long-tube case.

For the short-tube case, the boundary layer on the endwall of the tube is similar to that associated with the free disk, and the velocity distributions computed for the central region of the endwall are in good agreement with similarity solutions of the von-Kármán free-disk equations. Although this free-disk flow is controlled by E, rather than by E^*, the region of the disk over which this flow occurs increases with decreasing G and, hence, with decreasing E^*.

For the numerical solutions, the flow was assumed to be laminar; the agreement between the measured and computed velocity distributions implies that this is a valid assumption for values of E and E^* as small as 5×10^{-5} and 2.7×10^{-3}, respectively. No evidence was seen of turbulent self-induced flow, and no criterion is known for the transition from laminar to turbulent flow.

The effects of inlet conditions and tube geometry on self-induced flow are reported by Gilham, Ivey & Owen (1991), and a study of the heat-transfer problem will be reported elsewhere.

We wish to thank the Science and Engineering Research Council and Rolls Royce plc for funding the work reported in this paper. We are also indebted to Mr G. Harman and Mr C. Cross, of Rolls Royce plc, for posing such interesting questions and waiting patiently for some of the answers.

REFERENCES

Benton, E. R. 1966 On the flow due to a rotating disc. *J. Fluid Mech.* **24**, 781–800.

Brouwers, J. J. H. 1976 On the motion of a compressible fluid in a rotating cylinder. Doctoral thesis, University of Twente.

Cochran, W. G. 1934 The flow due to a rotating disk. *Proc. Camb. Phil. Soc.* **30**, 365–375.

Doormaal, J. P. Van & Raithby, G. D. 1984 Enhancements of the SIMPLE method for predicting incompressible fluid flows. *Numer. Heat Transfer* **7**, 147–163.

Ekman, V. W. 1905 On the influence of the earth's rotation on ocean-currents. *Ark. Mat. Astr. Fys.* **2**, 1–52.

Escudier, M. P. 1984 Observations of the flow produced in a cylindrical container by a rotating endwall. *Exps Fluids* **2**, 189–196.

Gilham, S. 1990 Theoretical study of self-induced flow in a rotating tube. D. Phil. thesis, University of Sussex.

Gilham, S., Ivey, P. C. & Owen, J. M. 1991 Self-induced flow in a stepped rotating tube. *ASME Intl Gas Turbine Conf., Orlando, Paper* 91-GT-276.

GOSMAN, A. D., KOOSINLIN, M. L., LOCKWOOD, F. C. & SPALDING, D. B. 1976 Transfer of heat in rotating systems. *ASME Intl Gas Turbine Conf., New Orleans, Paper* 76-GT-25.

IVEY, P. C. 1988 Self-induced flow in a rotating tube. D.Phil. thesis, University of Sussex.

KÁRMÁN, TH. VON 1921 Über laminare und turbulente Reibung. *Z. Angew. Math. Mech.* **1**, 233–252.

OWEN, J. M. & PINCOMBE, J. R. 1981 Rotationally induced flow and heat transfer in circular tubes, *University of Sussex Rep.* 81/TFMRC/32. School of Engineering and Applied Sciences, University of Sussex.

OWEN, J. M. & ROGERS, R. H. 1989 *Flow and Heat Transfer in Rotating-Disc Systems. Volume I: Rotor-Stator Systems.* Taunton: Research Studies Press.

PATANKAR, S. V. 1980 *Numerical Heat Transfer and Fluid Flow.* McGraw-Hill.

PATANKAR, S. V. & SPALDING, D. B. 1972 A calculation procedure for heat and mass transfer in three-dimensional parabolic flows. *Intl J. Heat Mass Transfer* **15**, 1787–1806.

SCHLICHTING, H. 1979 *Boundary-Layer Theory.* McGraw Hill.

STEWARTSON, K. 1957 On almost rigid rotations. *J. Fluid Mech.* **3**, 17–26.

VAUGHAN, C. M., GILHAM, S. & CHEW, J. W. 1989 Numerical solutions of rotating disc flows using a non-linear multigrid algorithm: *Proc. 6th Intl Conf. on Numerical Methods in Laminar and Turbulent Flow*, vol. 6, pp. 63–73. Swansea: Pineridge.